

MODELLING AND SIMULATION OF AN MR BRAKE BASED ON TORQUE COMPENSATION

Li Dongheng^{a,c}, Saiful Anuar Abu Bakar^{a*}, Mohamed Hussein^b, Wei Jigan^c, Tang Jiatian^c, He Yinhuan^c

^aAutomotive Development Center, Faculty of Mechanical Engineering, Universiti Teknologi Malaysia, Johor Bahru 81310, Malaysia

^bFaculty of Mechanical Engineering, Universiti Teknologi Malaysia, Johor Bahru 81310, Malaysia

^cSchool of Mechanical Engineering, Liuzhou Vocational & Technical College, Liuzhou, Guangxi 545006, P. R. China

Article history

Received

22nd January 2024

Received in revised form

29th February 2024

Accepted

3rd March 2024

Published

29th December 2024

*Corresponding author
saifulanuar@utm.my

ABSTRACT

A new design for a repetitive compression magnetorheological (MR) brake has been introduced, aiming to enhance both the efficiency and safety of vehicle safety systems, thereby accelerating the commercial adoption of such brakes in the automotive industry. This innovative brake uses a hybrid operational mode, replacing the conventional rotary motion with a unique recessive structure to enhance the braking performance. In the non-braking state, the design maintains the fluidity of the MR fluid, while in the braking state, it leverages the brake disc's recessive movement. Additionally, the study incorporates a temperature compensation mechanism to mitigate potential performance variations due to temperature changes. A three-dimensional static magnetic field analysis confirmed the magnetic circuit design's effectiveness and the suitability of the selected parameters and materials. The simulation showed that the brake's average magnetic field intensity rose by 145.26% when increasing the current from 1A to 4A, achieving a maximum braking torque of 51.4 Nm.

KEYWORDS

Brake-by-wire system, reverse extrusion, magnetorheological brake, temperature compensation, electromagnetic field simulation

INTRODUCTION

Nowadays, The brake-by-wire system has gained significant attention in the automotive-related research field due to the advanced progress of society and constant innovation in the vehicle industry. Magnetorheological (MR) fluids, a novel substance with distinctive rheological properties, have garnered significant attention in this technical field [1]. When subjected to an external magnetic field, MR fluid rapidly adopts a chain-like structure, exhibits characteristics similar to a solid, and generates a greater yield stress. The primary benefit lies in the ability to manipulate the rheological characteristics of MR fluids by modulating the intensity of the magnetic field. Furthermore, the fluidity of the MR fluids may be rapidly reinstated once the magnetic field is eliminated. The application of MR fluid in modern automotive brake-by-wire systems has extensive potential due to this property [2-5].

In contrast to the conventional disc or drum mechanical brake design, the MR brakes utilize MR fluid as the braking medium, eliminating the need for conventional mechanical components like vacuum pumps, pistons, and oil lines [6]. The MR brakes offer several advantages, including simplified control, compact structure, and reduced energy consumption, making the fluid a highly valuable technology in the automotive industry. Considering the limitations imposed by installation size and the demand for lightweight design, MR brakes must strike a balance between compactness and the ability to generate sufficient braking torque [7]. Typically, MR brakes are

classified into disc or drum types based on their design, which is determined by the shape of the rotor or the magnetic flux path. Over the past decade, researchers have developed various types of MR brakes with distinct structural configurations, aiming to achieve higher braking torque, reduced mass or volume, and lower power consumption[8-10]. Typically, Nguyen *et al.* [11] have developed a new type of brake based on the zigzag magnetic flux path. By using non-magnetic separator plates to separate the magnetic plates on the disc from each other, this design is lighter and more compact while providing the same braking torque according to experimental results. Shiao & Kantipudi [12] have developed a dual-disc multi-pole MR brake, which arranges six sets of coils between the left and right brake discs. The final braking density reaches 79.3 Nm dm^{-3} , which is higher than that of traditional disc brakes. Chen *et al.* [13] designed a dual-disc MR brake and utilized shape memory alloy springs to adjust the working gap of the MR fluid, and the experimental results showed that adjusting the gap, rather than modifying the current, could effectively reduce energy consumption while increasing the braking torque. Bazargan-Lari [14] has introduced a novel MR brake and the Nelder-Mead optimization algorithm, parameters optimization. The studies demonstrated that the MR working gap and brake

disc size have a promoting effect on improving brake performance.

This study proposes an innovative reciprocating-squeeze MR brake that applies damper design principles, using the MR fluid's high-strength properties in compression mode to efficiently engage the passive disc. The study meticulously addresses the impact of temperature fluctuations on the efficacy of MR fluids, integrating a sophisticated temperature compensation mechanism to assure consistent performance stability. Additionally, precise static magnetic field simulations performed with ANSYS Workbench software offer a detailed analysis of magnetic field distribution variations across the brake design's components under various current conditions.

DESCRIPTION OF THE PROPOSED MR BRAKE

Structure Design

The exploded view of the reciprocating MR brake, shown in Figure 1, primarily includes components like the outer casing, brake shaft, brake disc, passive disc, excitation coil, MR fluid, and flow regulation assembly.

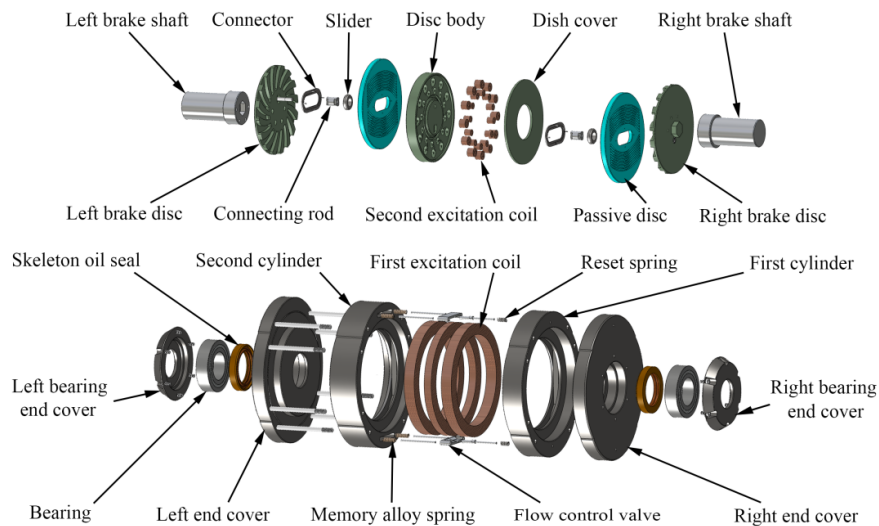


Figure 1: Explosion diagram of the proposed MR brake

To The sectional view depicted in Figure 2 reveals a pair of protrusions on each inner wall of the brake's cylindrical body, located within the squeeze slots and arranged oppositely. The space between these protrusions forms a connecting port that links the two squeeze slots. Additionally,

two connecting channels are strategically positioned along the cylinder's axis, each linking the squeeze slots at either end.

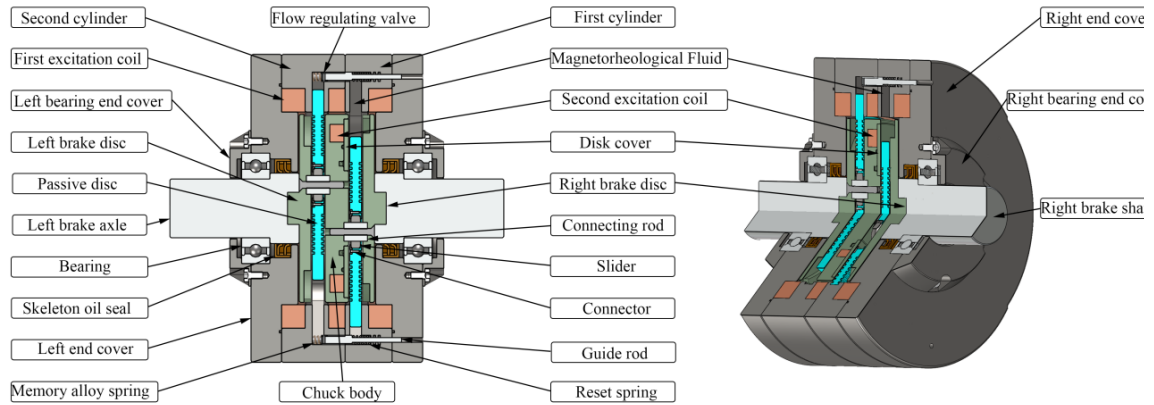


Figure 2: Sectional view of the proposed MR brake

The MR brake's shaft features a bifurcated design, with each segment parallel to the outer casing and rotatable. The left and right shafts are connected to the bearing holes of the end cap via a bearing assembly that includes oil seals, ensuring effective sealing and facilitating smooth rotation. The brake disc is divided into three sections: left, middle, and right, arranged consecutively within the brake cavity. Centrifugal blades are mounted on the outer surfaces of the left and right brake discs, which are firmly attached to their respective shafts, forming compression chambers. These chambers interconnect via channels in the exterior casing. The gap between the brake disc, passive disc, and housing is filled with MR fluid. This fluid circulates through the gaps between the outer casing's inner walls and the brake and passive discs, including the squeezing slots, connecting channels, and ports. The MR fluid's working gap is set at 0.5mm in this study, considering manufacturing practicalities.

Figure 3 shows the exploded view of the middle brake disc. A second excitation coil is strategically installed on the middle brake disc to enhance the magnetic field's intensity and even out its distribution within the MR fluid. The disc consists of a body and a cover, each with multiple fixed slots designed for the coil's installation and secure attachment. The body includes a central projecting shaft and a main section. Multiple fixed slots are evenly distributed and interconnected via

connecting slots along the end face of the shaft in the main section.

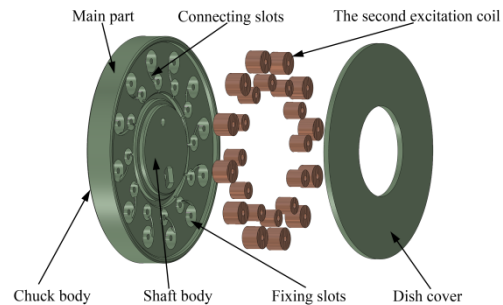


Figure 3: Structural drawing of the middle brake disc

Figure 4 presents the connection schematic of the brake disc and passive discs. Two passive discs are located in two squeeze chambers, each connected to an adjacent brake disc through connectors. As the brake disc rotates, the passive discs perform reciprocal radial movements along the brake shaft, moving in opposite directions to each other. The connectors, comprising connecting rods and sliders affixed to them, transform the rotational movement of the brake disc into a linear reciprocating motion of the sliders along the brake disc's radial direction. Each passive disc's end face has two sets of grooves, arranged on either side of the sliding holes. These grooves are arc-shaped, with the two sets protruding in opposite directions.

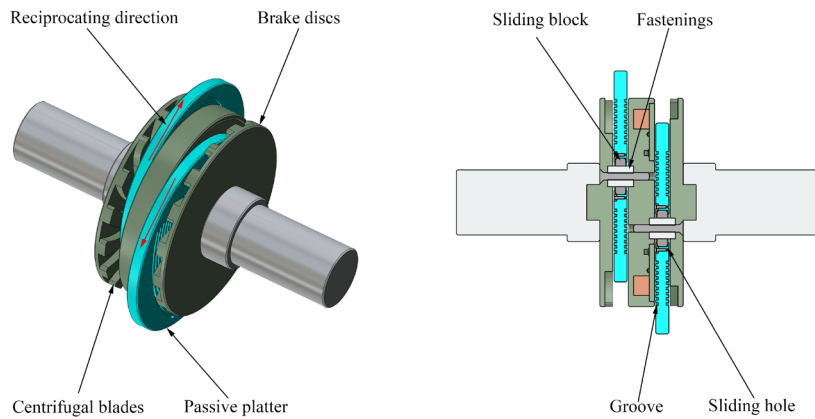


Figure 4: Schematic diagram of the connection between brake disc and passive disc

A side-mounted design is utilized for the three main excitation coils to reduce the weight and rotary diameter of the brake. Each coil is wound around the outer circumference of the brake discs and secured within its corresponding mounting grooves. The flow regulation assembly comprises a flow control valve and a shape-memory alloy spring. The flow control valve slides within the connecting channel, creating a passage for the MR fluid. The shape-memory alloy spring is situated at the end of the flow control valve, where it contacts both the main body section and the groove wall of the squeezing chamber. The valve moves within the connecting channel, transitioning from fully open to completely closed states. One end of the valve's main body features an inclined surface facing the squeezing chamber.

The reset component, incorporating a reset spring, is mounted on both sides of the flow control valve. As the MR fluid's temperature drops, the valve automatically reverts to its original position. The reset component is securely fastened to a guide rod, making contact with both the inner wall of the cylinder body and the main body part. Its expansion direction aligns with the braking shaft's axial direction. Furthermore, the flow regulation assembly features a traction element to modify the flow valve's motion, enabling regulation of the flow port's dimensions between its fully open and closed states. The pulling component, typically made of steel wire, is securely attached to the flow control valve's guide rod at one end and extends from the casing for convenient operation. The pulling component exits the casing through a through-hole in the end cap, providing the capability to adjust the system.

Working Principle

Support Vector Machine (SVM) is a machine learning-based energy management strategy. It is a supervised learning model in machine learning used in this research to optimize the HEVs' energy management. The support-vector machine is used to analyze data for classification and regression analysis [13, 14, 15]. It is used to train the data provided and then to predict the operation mode after constructing the model in Matlab-Simulink.

When the excitation coils are unpowered, the MR brake stays non-braking. Under these circumstances, the brake shaft's rotation simultaneously drives the three brake discs. The rotation causes the passive discs to oscillate along the brake shaft. At this stage, the temperature of the MR fluid remains constant, and the flow control valve is fully open, allowing maximum opening of the flow ports between the two squeezing chambers. The limited braking torque in this state is primarily due to the intrinsic viscosity of the MR fluid, bearing friction, and seals. These factors minimally impact the vehicle's performance.

During braking, the first excitation coil may be energized alone or together with the second coil to produce an adjustable magnetic field in the working gap filled with MR fluid. The brake discs' rotation causes the passive discs to reciprocate vertically, pressurizing the MR fluid to enhance braking torque. Figure 5 displays the structural schematic of the flow control valve. An increase in the MR fluid's temperature during braking can reduce the applied braking force. In response, the temperature-sensitive shape-memory alloy spring modifies the flow control valve, reducing the opening size in the flow port. This modification increases resistance to the flow of MR fluid in the squeeze chambers, thereby compensating for the reduced braking efficiency due to increased

temperature. As the MR fluid temperature falls, the shape-memory alloy spring returns to its initial position. However, when the flow control valve

only contacts the spring, a reset spring is required to restore the valve to its initial position.

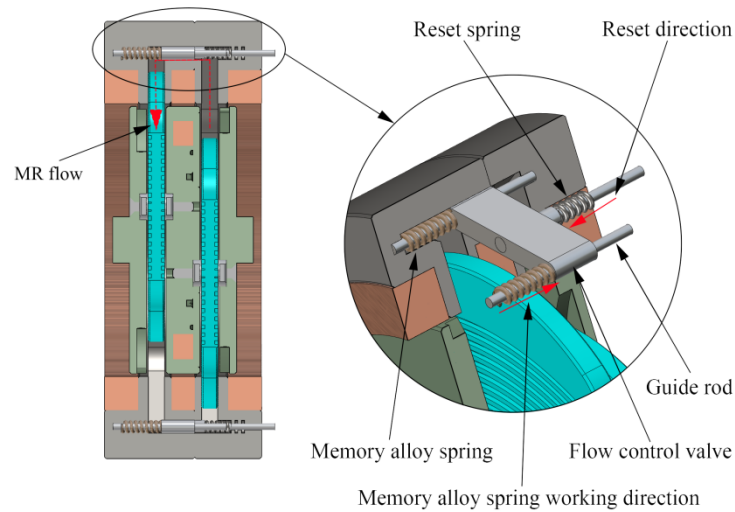


Figure 5: Structural schematic of the flow control valve

Once the braking process ends, the first excitation coil is de-energized, returning the MR fluid to its liquid state. In the event of an unexpected power outage, the excitation coils will lose their magnetic field. Under such circumstances, the flow control valve can be quickly closed by pulling the actuator, increasing flow resistance and enabling emergency braking to enhance equipment safety. Furthermore, by adjusting the actuator's position, the braking torque can be modified as needed. The passive discs feature grooved surfaces, and centrifugal blades on the brake discs' ends stir the MR fluid, preventing it from settling and layering during prolonged inactivity, thereby maintaining braking efficiency. This design ensures the MR fluid remains effective in braking performance by preventing sedimentation and layering, even after long periods of inactivity.

MATHEMATICAL MODEL

Figure 6 illustrates the structural properties of the brake. The output braking torque of the MR brake during braking comprises three main components: viscous resistance torque from the MR fluid's inherent viscosity with the coil unpowered, shear torque from the MR fluid under the magnetic field with the coil powered, and resistance torque from the passive disc's movement overcoming the MR fluid's yield stress. To simplify calculations, the following assumptions address the MR brake's complex operational conditions:

- (1) The MR fluid is incompressible;
- (2) The MR fluid fills the working gap and is evenly distributed, ignoring gravity and centrifugal force effects on the fluid's soft magnetic particles;
- (3) Temperature effects on the MR fluid's properties are disregarded.

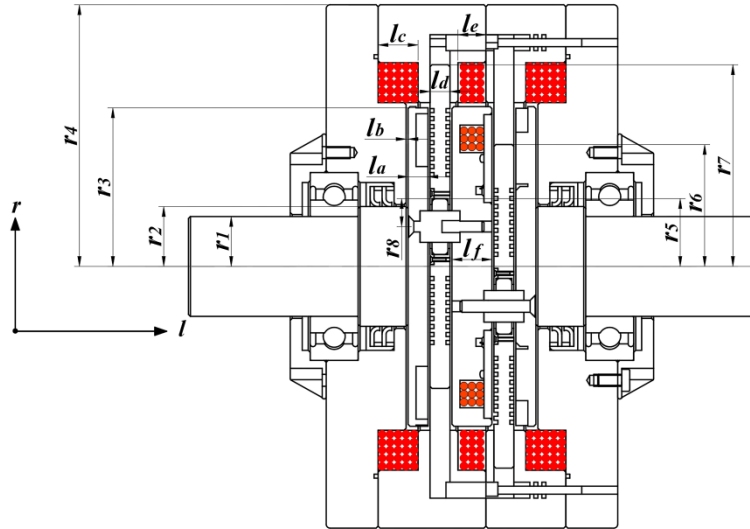


Figure 6: Geometrical parameters of the proposed MR brake

The braking torque generated by the MR fluid between the brake disc and the left and right casings can be expressed as

$$T_r = \frac{4\pi\tau_B(r_3^3 - r_2^3)}{3} + \frac{\pi\eta\omega(r_3^4 - r_2^4)}{l_b} \quad (1)$$

where τ_B is the shear yield stress of the MR fluid at the working gap, r_3 and r_2 are the outer and inner radius of the brake disc respectively, η is the zero-field viscosity of the MR fluid, ω is the rotational

speed of the brake disc, and l_b is the thickness of the MR fluid at the working gap.

Both the braking and passive discs are of the same size. As shown in Figure 7, the actual working area for the MR fluid is formed by the overlapping region between the brake disc and the passive disc, assuming an offset distance from the brake disc, denoted as h , when the passive disc undergoes reciprocating motion.

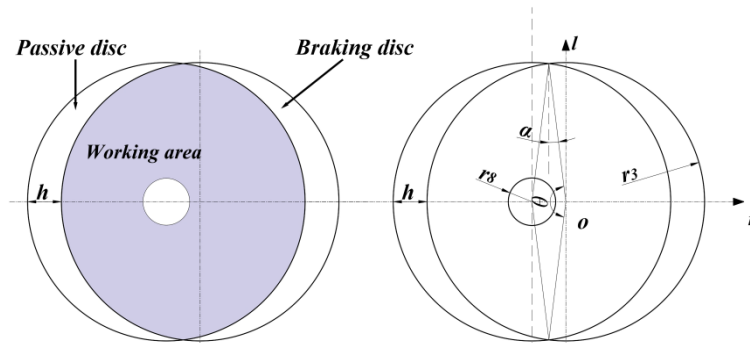


Figure 7: Overlapping region between the brake disc and the passive disc

Some The spatial extent of this working area can be expressed as

$$\Delta A = r_3^2 \cos^{-1}\left(\frac{h}{2r_3}\right) - h\sqrt{r_3^2 - \left(\frac{h}{2}\right)^2} - \pi r_8^2 \quad (2)$$

where r_8 is the radius of the sliding block.

The resistance generated by magnetostriction can be expressed as

$$F_\eta = \Delta A \tau_B \quad (3)$$

When h equals 0, indicating the alignment of the radial heights of the brake disc and the passive disc, the resistance generated by the magnetically induced pressure drop can be represented as follows

$$F_\eta = \pi\tau_B(r_3^2 - r_8^2) \quad (4)$$

During the motion of the passive disc, the resistance generated is transmitted to the rotational shaft as braking torque through the connecting block. This braking torque can be quantified as follows

$$T_d = 4F_\eta \cdot r = \frac{4\pi\tau_B (r_3^3 - r_3 r_8^2) r_8}{l_b} \quad (5)$$

The braking torque generated by the MR fluid in the working gap between the brake disc and the passive disc can be represented as follows

$$T_m = \frac{8\pi\tau_B (r_3^3 - r_8^3)}{3} + \frac{2\pi\eta\omega (r_3^4 - r_8^4)}{l_b} \quad (6)$$

In summary, the total braking torque produced by the MR fluid can be expressed as follows:

$$T_s = T_d + T_m + T_r \quad (7)$$

STATIC MAGNETIC FIELD SIMULATION

In the static electromagnetic field analysis, the magnetic flux leakage effects from the brake structure, including the casing and shaft, are ignored. It is assumed that the magnetic field is fully contained within the model. The main parameters of the brake are shown in Table 1. The MR brake model is defined by an exterior barrier that serves as a parallel limiting interface for magnetic flux. The current density excitation presents the main challenge in simulations. The initial excitation coil in this study is wound with enamelled copper wire of 1mm diameter and comprises 100 turns. The second coil features 70 turns.

Table 1: Main parameter of the proposed brake

Symbol	Value	Symbol	Value
r_1	12.5mm	r_8	7mm
r_2	15mm	l_a	5mm
r_3	40mm	l_b	5mm
r_4	65.5mm	l_c	10mm
r_5	17mm	l_d	5mm
r_6	30mm	l_e	7mm
r_7	50mm	l_f	10mm

A precise finite element model is crucial for conducting static magnetic field analysis. The brake model in this study was simplified by

omitting small features such as screw holes and chamfers on the cylinder and end caps. These features were considered as a continuous entity. The simplified three-dimensional model was imported into ANSYS Workbench for analysis. The simulation uses pure copper for the coil material, Q235 steel for the casing, disc, and other components, and a copper alloy for the shaft. This work treats Q235 steel and MR fluid (MRF-350) as nonlinear magnetic materials, with their B-H curves shown in Figure 8.

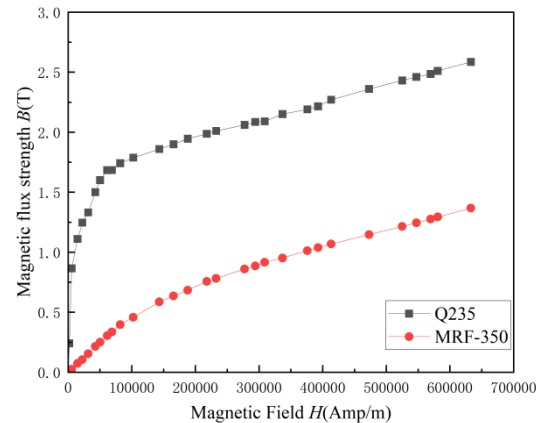


Figure 8: B-H Curve of Q235 and MFR-350

The mesh division must accurately represent the analysis model to ensure the accuracy of finite element analysis. Coarse meshing may distort results, whereas finer meshing improves solution precision. In this study, hexahedral elements are used for the coils, and tetrahedral elements are employed for other components. The geometric model is divided into 74,821 elements with 165,112 nodes. ANSYS offers more than ten mesh quality control parameters, and in this study, element quality is selected as the key metric. This choice enables quick identification and resolution of element quality issues, enhancing analysis precision, reducing computational errors, and more accurately predicting structural performance and behavior. Mesh sizes are set at 5mm for the casing, 2mm for the MR fluid, and 4mm for other components. The mesh division results are shown in Figure 9.

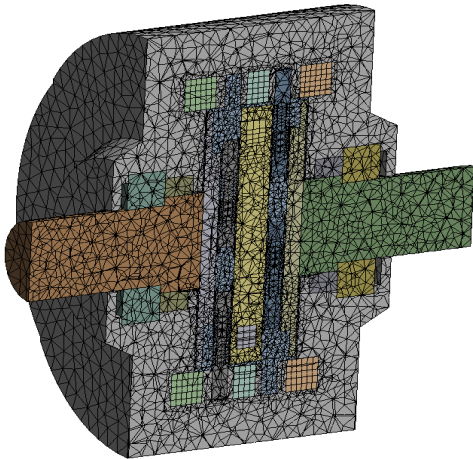


Figure 9: Mesh of the proposed MR brake

Figure 10 illustrates the spatial distribution of the magnetic flux density vector in the brake with a 4A current applied. The diagram shows the trajectory of the magnetic field lines as they traverse the brake's casing, active disc, passive disc, MR fluid, and the working gap, creating a closed circuit around the brake disc. The magnetic circuit design of the MR brake, along with the careful selection of component materials, ensures a logical and efficient facilitation of a homogeneous magnetic field distribution. This uniformity's consistency guarantees the braking mechanism's reliability and effectiveness.

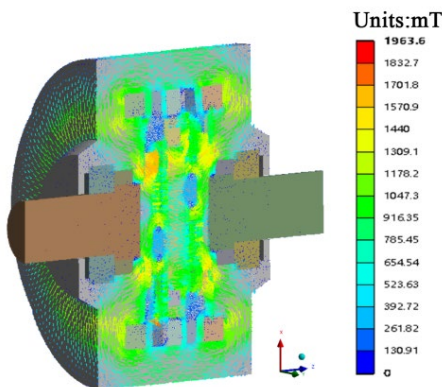


Figure 10: Magnetic flux density vector of the proposed MR brake

When the number of turns in the excitation coil and the MR fluid working gap remains constant, changes in the excitation current substantially impact the brake's overall magnetic field distribution. Figure 11's cloud diagram shows the brake's magnetic field distribution at excitation currents of 1A, 2A, 3A, and 4A. The diagram indicates that the brake's highest magnetic field is located near the second excitation coil. The magnetic field values at these currents are 1.7920T, 1.8930T, 1.9373T, and 1.9636T, respectively. This phenomenon results from the high concentration of magnetic field lines in that region, leading to an intensified magnetic force. In contrast, the magnetic field intensity near the brake's rotating shaft and the coil placements is almost negligible. The reason is that the revolving shaft, made of a non-magnetic material, minimally affects the magnetic field. Additionally, the coil's internal field counteracts its generated magnetic field, reducing intensity within the coil. As the excitation current increases, the color density in the magnetic field cloud diagram shifts from lighter to darker, indicating an increase in the brake's total magnetic field intensity. The brake's average magnetic field rises from 0.2433T to 0.5999T, marking a 145.26% increase. This indicates a significant amplification of the magnetic induction intensity across the entire braking zone, especially in the crucial working areas around the MR fluid, where the increase in magnetic field strength is more pronounced.

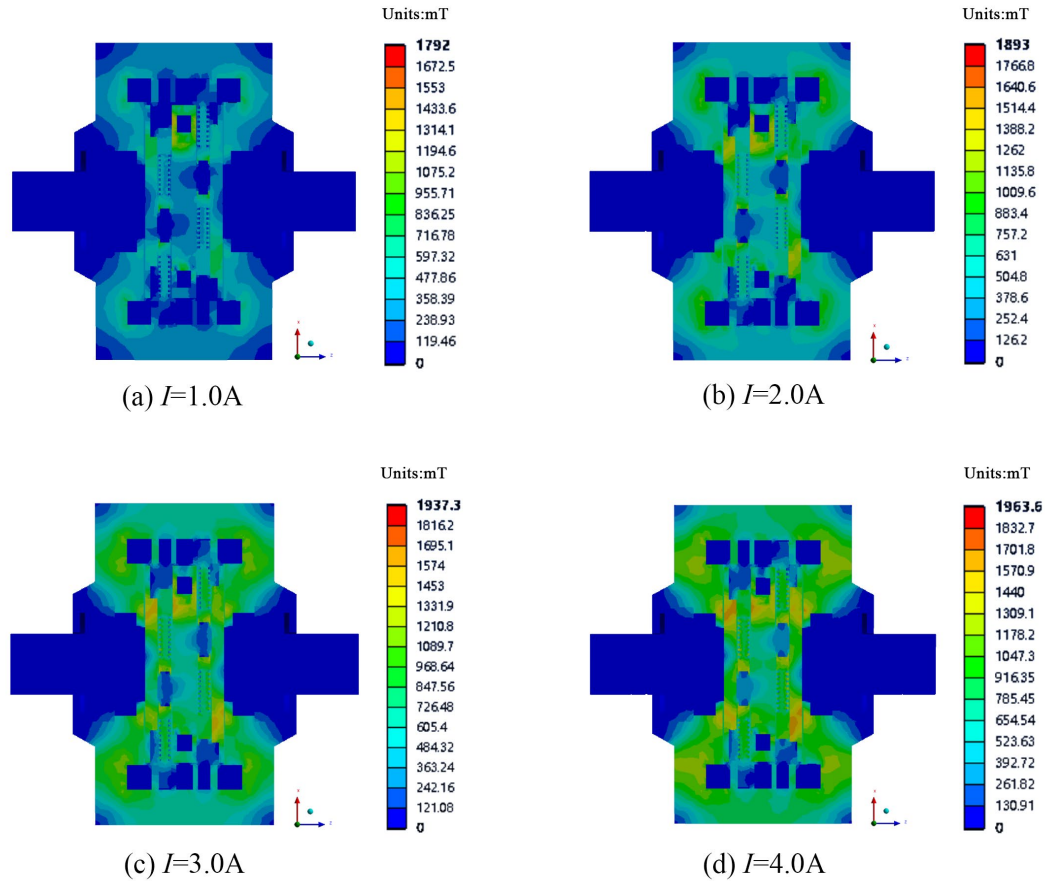


Figure 11: Magnetic field distribution of the MR brake under different currents

Figure 12 displays the distribution of magnetic induction intensity in the MR fluid at excitation currents of 1A, 2A, 3A, and 4A. The results demonstrate a consistent and even distribution of magnetic induction intensity across the working gap, showing radial symmetry along the center axis. The magnetic induction strength progressively increases from the center toward the outer region, with a slight decline in the outermost layer. At excitation currents of 1A, 2A, 3A, and 4A, the maximum induction intensities in the working

gap are approximately 0.5063T, 0.7981T, 0.9891T, and 1.1547T, respectively. These maximum intensities occur in the region where the middle brake disc contacts. Multiple coils in the middle brake disc significantly augment the magnetic field intensity. When the excitation current exceeds 4A, the magnetic induction intensity in the MR fluid nears its saturation point. This suggests that with the progressive rise in current, the rate of increase in the magnetic field strength will gradually diminish, reaching a point where it no longer rises.

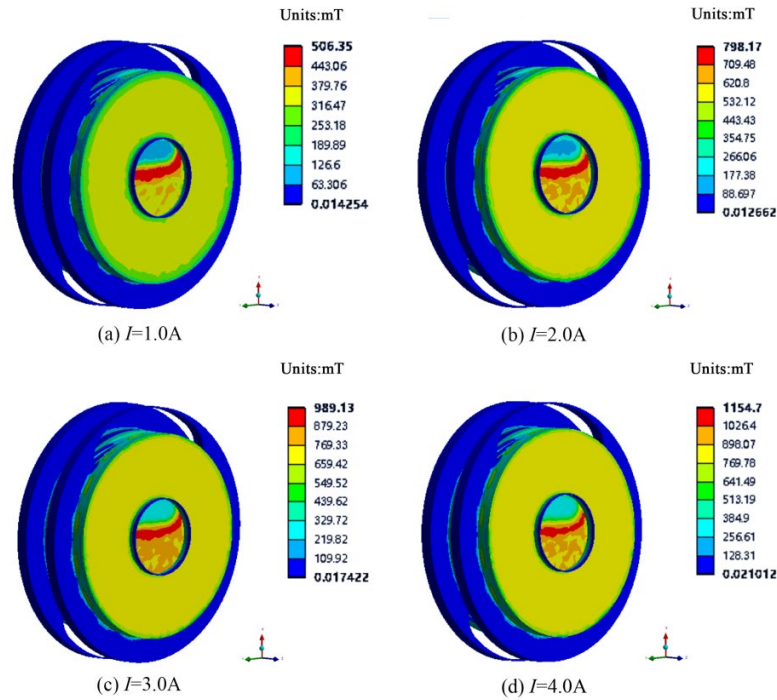


Figure 12: Magnetic field distribution of the MR fluid under different currents

Furthermore, the relationship between current and magnetic induction intensity in the working gap is analyzed, and the average magnetic induction intensity B in the working gap can be expressed as

$$\bar{B} = \frac{\int B_x dx}{\int dx} \quad (8)$$

Figure 13 illustrates the correlation between magnetic induction intensity and current within MR fluid. Increasing the excitation current boosts the magnetic potential in the magnetic circuit, resulting in a higher average magnetic induction intensity inside the working gap. However, the rate of increase in magnetic field strength differs

between the inner and outer layers of the MR fluid working gap. The MR fluid's outer layer, between the brake disc and the casing, exhibits a more pronounced increase in magnetic field intensity. This is due to multiple small coils improving the inner layer's magnetic field of the MR fluid's working gap, while the passive disc and brake disc's surface blades increase magnetic reluctance. Consequently, this disrupts the magnetic field strength in that specific region. Nevertheless, the magnetic field strength is generally evenly distributed across both the inner and outer layers of the MR fluid working gap. This distribution matches the growth trend of the B-H curve of the MR fluid used in the simulation

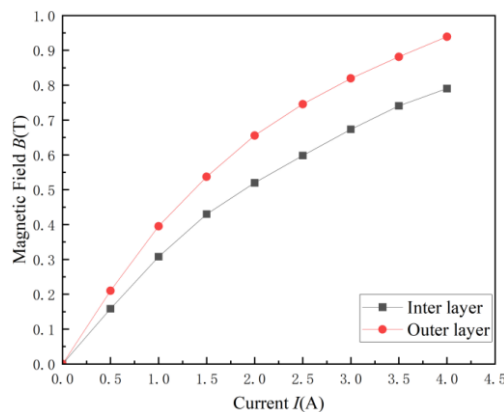


Figure 13: Magnetic field density versus coil current

Equation (7) predicts the braking torque of the designed MR brake based on simulation data. Figure 14 illustrates the relationship between braking torque and applied current at 200 rpm. The braking torque peaks at approximately 51.4 N·m. Additionally, the current and braking torque relationship is modeled using the Broyden-

Fletcher-Goldfarb-Shanno (BFGS) algorithm and a general global optimization approach, as equation (9) shows.

$$T_s = \frac{45.8148(I^2 + 2.6309I)}{I^2 + 0.9068I + 3.9831} \quad (9)$$

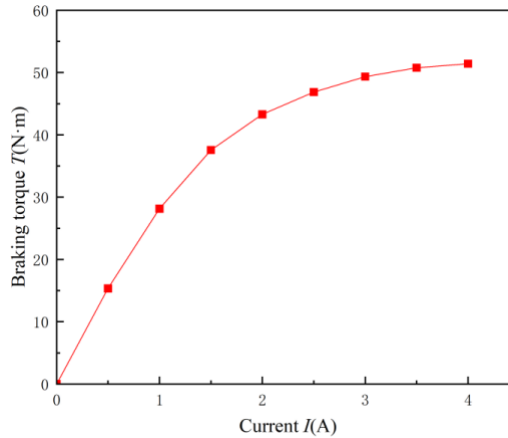


Figure 14: Braking torque versus coil current

Initially, the data indicate an increase in braking torque with rising applied current, mirroring the magnetic field strength's increase with current. Within the 0-2A current range, the increase in braking torque exhibits a predominantly linear pattern, with the torque at 2A being 2.8 times greater than that at 0.5A. As the current increases from 2 A to 3 A, the rate of increase in braking torque diminishes. Ultimately, when the current reaches 4 A, there is minimal additional improvement in braking performance. At this level of magnetic flux density, the shear stress approaches its maximum capacity, leading to minimal enhancement in braking ability with increased current.

IMPACT OF MESH AND NODE SIZES ON SIMULATION

Given that braking torque calculation mainly depends on the MR fluid's magnetic field strength in the working gap, this study examines the impact of grid size and node count on electromagnetic field simulation outcomes. For instance, at a 3.0 A excitation current, the previous section set the MR fluid's grid size to 2 mm. Since the MR fluid

significantly impacts the MR brake's results, only the MR fluid's grid size was reduced to 1mm, keeping other grid sizes and partitioning methods constant. After the grid size adjustment, elements and nodes increased to 217,327 and 455,679, respectively, marking increases of 190.46% and 175.98% over the previous setup in Figure 9. Under the same computer conditions, simulation time rose from 9 minutes and 48 seconds to 33 minutes and 41 seconds, a 3.5-fold increase in computational time. Adjusted simulation results are shown in Figure 15. The overall brake distribution and MR fluid's local magnetic field follow a similar pattern to before the modification, with a slight increase in magnetic field strength. Maximum magnetic field values for the brake and MR fluid are 2.0303 T and 1.0057 T, respectively, showing increases of 4.8% and 1.6% over the 2 mm grid in Figures 11 and 12. Furthermore, average magnetic field values are 0.7412 T between the brake and passive discs, and 0.7158 T between the housing and passive disc, increases of 2.1% and 5.1%, respectively. Enhancing the MR fluid grid accuracy from a 2mm size yields an approximate 3% improvement in simulation but significantly reduces solving efficiency.

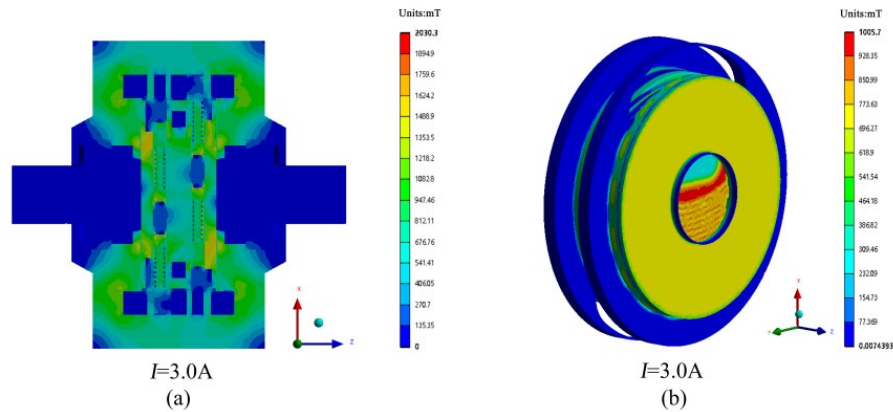


Figure 15: Magnetic field distribution of the (a) MR brake and (b) MR fluid

CONCLUSION

The MR brake, as proposed in this study, remains non-braking when not subjected to external stimulation, thus ensuring the stability of the MR fluid's temperature. The excitation current is adjusted to provide the necessary braking torque during the braking process. The distinctive design of the flow control valve allows it to automatically adapt to variations in MR fluid temperature, ensuring consistent and steady braking performance. Additionally, the brake design incorporates measures to prevent the stratification of MR fluid due to extended inactivity, thus ensuring the long-term reliability of braking performance. The simulation shows that an increase in excitation current results in a higher total magnetic field strength, while the number of excitation coil turns remains constant. The average magnetic field strength of the brake increased by 145.26% during the transition from 1A to 4A. The maximum braking torque achieved is 51.4 N·m. However, as the current increases, the rate of magnetic field expansion slows down due to magnetic saturation. Therefore, it is crucial to consider the influence of magnetic saturation when developing and implementing MR brakes, to avoid exceeding the MR fluid's ideal operating point. The brake system, designed with compact dimensions and relatively low braking torque, is specifically tailored for smaller, low-speed off-road vehicles. Illustrative instances encompass electric or gas-powered golf carts, characterized by dimensions around 2300mm in length, 12hp in power, and a weight of approximately 300kg. The advancement of MR brake systems for these compact vehicles is still in its early phases, and this particular design serves as a valuable reference for furthering the design and research of MR brake systems within this vehicular category.

The main scope for this study is the MR brake modelling. Future work will thoroughly investigate the flow field changes caused by the opening and closing of valves during the temperature variation process in the designed model, and the impact of mesh quality on the accuracy of simulation results will be further explored through experimental studies. Additionally, an analysis will be conducted on the actual correlation between the brake's temperature field and braking torque under various braking conditions, to establish a relationship between temperature and torque variations in the designed model.

ACKNOWLEDGEMENTS

The authors would like to acknowledge the support given by the Department of Aeronautics, Automotive and Ocean Engineering, Faculty of Mechanical Engineering, Universiti Teknologi Malaysia. This work was also supported by the 2023 Liuzhou Vocational and Technical College Project [grant number 2023KB04].

REFERENCES

- [1] Wang D. M., Yang G. X., Luo Y. J., Fang S. R., Dong T., (2023). Optimal design and stability control of an automotive magnetorheological brake considering the temperature effect. *Smart Materials and Structures*. 32(2): 025020. <https://dx.doi.org/10.1088/1361-665X/acb1e2>.
- [2] Shamieh H., Sedaghati R., (2018). Development, optimization, and control of a novel magnetorheological brake with no zero-field viscous torque for automotive applications. *Smart Materials and Structures*. 29(16): 3199-213. <https://dx.doi.org/10.1088/1361-665X/aa9452>.
- [3] Patil S. R., Sawant S. M., (2018). Experimental Studies on Magnetorheological Brake for Automotive Application. *Int. J. Automot. Mech. Eng.* 15(1): 4893-

908.
<https://dx.doi.org/10.15282/ijame.15.1.2018.2.0381>.
- [4] Kalikate S. M., Patil S. R, Sawant S. M., (2018). Simulation-based estimation of an automotive magnetorheological brake system performance. *Journal of Advanced Research*. 14: 43-51. <https://dx.doi.org/10.1016/j.jare.2018.05.011>.
- [5] Shamieh H., Sedaghati R., (2017). Multi-objective design optimization and control of magnetorheological fluid brakes for automotive applications. *Smart Materials and Structures*. 26(12): 125012. <https://dx.doi.org/10.1088/1361-665X/aa9452>.
- [6] Wu J., Deng B., Huang Y., Zhang H., Tang S., (2022). A multi-pole magnetorheological clutch powered by permanent magnets and excitation coils. *Journal of Intelligent Material Systems and Structures*. 34(2): 217-28. <https://doi.org/10.3390/act11050120>.
- [7] Singh R. K., Sarkar C., (2023). Two-wheeler magnetorheological drum brake operating under hybrid mode for enhancing braking torque: Development and validation. *Mechatronics*. 92: 102971. <https://dx.doi.org/10.1016/j.mechatronics.2023.102971>.
- [8] Thakur M. K., Sarkar C., (2021). Investigation of Different Groove Profile Effects on Torque Transmission in Shear Mode Magnetorheological Clutch: Numerical Simulation and Experimental Study. *Journal of Tribology*. 143(9): 091801. <https://dx.doi.org/10.1115/1.4049255>.
- [9] Nguyen V. B., Le H. D., Nguyen QH, Duyen DQ, Hieu DHM, Choi S-b., (2021). Design and experimental evaluation of a novel magneto-rheological brake with tooth-shaped rotor. *Smart Materials and Structures*. 31(1): 015015. <https://dx.doi.org/10.1088/1361-665X/ac38ff>.
- [10] Ye F., Peng D., Yuan Y., Wang X., Qing O., (2020). Multi-objective optimization design and performance evaluation of T-shaped magnetorheological brake. *Journal of Simulation*. 8(4): 88-91. <https://doi.org/10.3390/act11050120>.
- [11] Nguyen Q. H., Nguyen V. B., Le H. D., Duyen D. Q., Li W., Hung N. X., (2021). Development of a novel magnetorheological brake with zigzag magnetic flux path. *Smart Materials and Structures*. 30(12): 125028. <https://dx.doi.org/10.1088/1361-665X/ac3430>.
- [12] Shiao Y. J, Kantipudi M. B., (2021). High torque density magnetorheological brake with multipole dual disc construction. *Smart Materials and Structures*. 31(4) 045022. <https://dx.doi.org/10.1088/1361-665X/ac5860>.
- [13] Chen W., Xiong Y., Shu R., Huang J., (2022). Analysis and experimentation of an adjustable gap magnetorheological brake controlled by electrothermal shape memory alloy spring. *Journal of the Brazilian Society of Mechanical Sciences and Engineering*. 44(8): 358. <https://dx.doi.org/10.1007/s40430-022-03657-x>.
- [14] Bazargan-Lari Y., (2019). Design and shape optimization of MR brakes using Nelder–Mead optimization algorithm. *Mechanics & Industry*. 20(6): 602. <https://dx.doi.org/10.1051/meca/20190>